

Resolving the Metastable Si-XIII Structure through Convergent Theory and Experiment

Fabrizio Rovaris^{a,1}, Corrado Bongiorno^{d,1}, Anna Marzegalli^a, Mouad Bikerouin^{a,g}, Davide Spirito^f, Gerald J. K. Schaffar^c, Mohamed Zaghoul^d, Agnieszka Anna Corley-Wiciak^h, Francesco Montalenti^a, Verena Maier-Kiener^c, Giovanni Capellini^{b,e}, Antonio M. Mio^d, Emilio Scalise^{a,*}

^a*Department of Materials Science. University of Milano-Bicocca, Via R. Cozzi 55, 20125, Milano, Italy*

^b*IHP-Leibniz Institute for High Performance Microelectronics, Im Technologiepark 25, 15236, Frankfurt(Oder), Germany*

^c*Department of Materials Science. Montanuniversität Leoben, Roseggerstrasse 12, 8700, Leoben, Austria*

^d*Institute for Microelectronics and Microsystems (IMM). Consiglio Nazionale delle Ricerche (CNR), Strada VIII 5, 95121, Catania, Italy*

^e*Department of Sciences. Università Roma Tre, V.le G. Marconi 446, 00146, Rome, Italy*

^f*BCMaterials. Basque Center for Materials, Applications and Nanostructures, UPV/EHU Science Park, 48940, Leioa, Spain*

^g*Aalto University, Engineered Nanosystems Group, P.O. Box 13500, FI-00076, Aalto, Finland*

^h*European Synchrotron Radiation Facility, Cedex 9, 38043, Grenoble, France*

Abstract

Silicon is the undisputed cornerstone of modern technology, with applications ranging from micro- and opto-electronics to quantum technologies. Recently, the exploration of its allotropes has emerged as a pivotal frontier for engineering materials with tailored optical and electronic functionalities. High-pressure experiments have revealed several metastable silicon phases, among which is Si-XIII. First observed more than 20 years ago, this phase has remained structurally unidentified, representing a significant gap in our understanding of elemental silicon allotropy. In this work, a convergent methodology is employed combining advanced theoretical modeling with experimental characterization to finally resolve the long-standing structural assignment of Si-XIII. Guided by careful experimental observations, a structural model validated through first-principles optimization and systematically tested against multiple experimental signatures is constructed. All the fingerprints of this phase are rationalized by our proposed crystal structure: interplanar spacings, Raman frequencies, thermodynamic stability, and kinetic pathways. These findings provide a crucial missing piece in the high-pressure phase diagram of silicon and demonstrate the power of integrating computational predictions with experimental validation to resolve complex structural problems in materials science.

Keywords: Si-XIII, Metastable silicon allotropes, Nanoindentation, TEM/SAED, Raman spectroscopy, Phase Transition, Kinetics

1. Introduction

Silicon (Si) has been the cornerstone of micro- and nanoelectronics for decades, with recent developments extending to optoelectronics and quantum technologies [1]. Despite being one of the most extensively studied semiconductors, fundamental questions regarding its elemental allotropy remain open, particularly in light of their potential use in technological applications. Indeed, while several different allotropic forms of Si have been identified [2, 3], the crystalline structure of several of its metastable phases reported in the literature, such as Si-VIII, Si-IX, and notably Si-XIII, remains elusive [2, 4].

*Corresponding author

Email address: emilio.scalise@unimib.it (Emilio Scalise)

¹These authors equally contributed

Beyond their fundamental interest, metastable silicon phases are increasingly recognized as a powerful lever for engineering the properties of silicon-based materials and devices. This is because they offer properties beyond those currently achievable with the "standard" CMOS technology based on (001)-oriented, diamond-cubic Si (*dc*-Si). As an example, some non-diamond allotropes have been predicted, and in some cases experimentally demonstrated, to exhibit reduced thermal conductivity [5], enhanced thermoelectric performance [6, 7], high carrier mobility [8], superconductivity [9], or even a direct and quasi-direct fundamental bandgap [10–12]. These properties open new technology routes for on-chip energy harvesting, integrated photonics and more exotic quantum functionalities. However, pressure-induced transformations can lead to wafer failure, defect generation and performance degradation under extreme conditions. Therefore, understanding the mechanical stress-driven nucleation mechanisms of these allotropes is crucial for unlocking new processing possibilities and enhancing material quality.

Therefore, identifying and decoding such metastable phases is one of the most complex and significant challenges in materials science. Intrinsically, these metastable phases are accessible only under specific non-equilibrium conditions, typically through high-pressure treatments like nanoindentation or diamond anvil cell (DAC) compression [4, 13]. Furthermore, stabilizing these phases often results in the formation of heterogeneous phase mixtures where the targeted allotropes coexist with, for example, amorphous silicon, diamond-cubic remnants, or other metastable structures, frequently organized in misaligned nanometric grains [13, 14]. This structural complexity makes interpreting experimental data, such as Raman spectra or diffraction patterns, particularly arduous when the underlying atomic structure is unknown. Resolving these ambiguities requires a rigorous synergistic approach between theory and experiment, cross-validating multiple characterization techniques with advanced theoretical modeling.

Such a convergent approach has been adopted here to finally resolve the crystalline structure of the long-debated Si-XIII phase, first uncovered over 20 years ago by Domnich *et al.* [15]. A bulk atomistic model is presented, achieving comprehensive agreement with all available experimental evidence. This model is supported by a solid theoretical framework describing the kinetics of phase transitions to and from this structure, as well as its relationships with the stable diamond-cubic (Si-I) and hexagonal-diamond (Si-IV) phases, and the well-known high-pressure R8 (Si-XII) and BC8 (Si-III) allotropes [13].

Through nanoindentation-based mechanical processing and controlled thermal treatment, a phase exhibiting the characteristic Raman signature of Si-XIII [4, 16] has been obtained. To unambiguously identify this structure, meticulous transmission electron microscopy (TEM) and selected area electron diffraction (SAED) analysis were performed. These analyses cross-referenced diffraction data from multiple zone axes to rule out compatibility with other known silicon allotropes and to isolate the specific volume transformed into the new phase. Building on these rigorous diffraction-derived descriptions of the crystal lattice, a first-principles approach was employed to refine candidate structures. This ultimately led to the identification of a configuration that is crystallographically consistent, energetically metastable, and whose computed Raman spectrum accurately reproduces the unique experimental signature of Si-XIII.

Beyond static structural validation, an advanced implementation of the solid-state dimer (SS-Dimer) method [17, 18] was employed, specifically tailored for crystalline solids, to map the kinetic pathways connecting the Si-XIII structure to both diamond phases (cubic Si-I and hexagonal Si-IV) as well as to the high-pressure R8 (Si-XII) and BC8 (Si-III) metastable phases. This approach allows us to identify physically-plausible transition pathways and associated energy barriers that are fully consistent with the mechanical loading and subsequent annealing conditions used in our experiments. In this way, the proposed Si-XIII structure is embedded into a coherent thermodynamic and kinetic framework that links its formation, stability, and kinetics to the broader high-pressure phase diagram of silicon, providing a comprehensive atomistic picture of the stress- and temperature-driven phase transformation landscape.

2. Results and Discussion

2.1. Structure of the Si-XIII phase

2.1.1. From SAED to the crystal structure

Numerous theoretical and experimental studies have attempted to identify and assign a crystal structure to the Si-XIII phase. However, it remains one of the few experimentally-identified silicon allotropes whose

crystalline structure remains unknown [16]. Experimental evidence consistently associates Si-XIII with characteristic Raman peaks at approximately 475 cm^{-1} and 330 cm^{-1} , together with electron-diffraction spots at $\sim 5.6\text{ \AA}$ and $\sim 4.4\text{ \AA}$, which cannot be attributed to any other known silicon phase [4, 15, 16, 19, 20]. Despite extensive literature on this elusive phase, most studies have been limited to identifying individual plane spacings, leaving no definitive assignment to a crystal structure that fully reconciles all experimental observations.

Here, we address this challenge through systematic TEM and SAED investigations of nanoindented silicon subjected to ramped thermal annealing up to 220°C . Building on the observation by Wong et al. [16] that ramped annealing protocols favor Si-XIII formation, we employed a staged thermal treatment that produces distinct diffraction signatures consistent with the Si-XIII patterns previously reported in the literature [16, 20], unlike isothermal furnace treatments at $\sim 250^\circ\text{C}$, which predominantly stabilize *hd*-Si [13]. To extract reliable structural information from electron diffraction, analogous to single-crystal X-ray diffraction protocols, we isolated individual grains and systematically acquired multiple low-index zone axes from the same crystallite, as schematically illustrated in Figure 1(a).

The procedure began by selecting a prominent unknown diffraction spot visible in the SAED pattern from the pit's inner region, as shown in Figure 1(a)-(c). Specifically, the spots positioned near the center of the pattern, indicated by a green circle in Figure 1(b) and relative to the interatomic distances of $4.3 - 4.6\text{ \AA}$, have frequently been reported in the literature as an indication of the presence of Si-XIII [16, 20]. An objective aperture was inserted to select this spot and generate a corresponding dark-field image, spatially locating the area of interest related to the unknown crystal structure, as reported in Figure 1(c).

From the dark field image, it is evident that the unknown phase is distributed throughout the entire pit area. The brighter grain in the dark field image (green circle in Figure 1(c)) was then selected, following its specific SAED response during the entire sample rotation procedure. The sample was then tilted around the axis parallel to the selected spot direction, maintaining it in Bragg condition until a low-index zone axis was reached. This orientation was set as the reference of the goniometer. Tilt series were then performed to span a total angle of $\sim 50^\circ$ (goniometer limit), following the same grain and maintaining the same spot in Bragg condition, i.e. rotating around the direction perpendicular to the (1-10) planes, continuously tracking additional zone axes while recording precise rotation angles. This generated comprehensive rotational maps of the reciprocal lattice, from which compatible Bravais lattice parameters could be inferred. A representative sequence of SAED patterns acquired from this grain is shown in Figure 1(d)-(g).

The zone axis morphologies and mutual angular relationships observed in the SAED patterns closely resemble those of the R8 structure (see simulated SAED patterns in Supporting Information, Figure S1), the metastable phase commonly formed during nanoindentation alongside BC8, as extensively discussed in the Raman spectroscopy section below and widely reported in the literature [4, 13, 15, 16, 19, 20]. However, the interplanar spacings and unit cell angles differ significantly from those of pristine R8. Guided by this structural similarity, we systematically explored distortions of the R8 unit cell, varying lattice constants and angles to match the measured diffraction data. This iterative process ultimately yielded a set of cell parameters producing very good agreement between calculated and experimental interplanar distances, zone-axis geometries, and rotation angles. Simulated SAED patterns from the proposed cell structure, shown in Figure 1(h)-(k) alongside their corresponding indexing, faithfully reproduce the experimental patterns. This agreement extends to both zone-axis geometries and relative reflection intensities.

2.1.2. DFT-Based structural determination of Si-XIII

Following this detailed SAED-based reconstruction of the reciprocal lattice and the identification of a distorted R8-like cell compatible with the experimental zone axes, we used Density Functional Theory (DFT) to refine and validate candidate atomic structures. Taking the R8 unit cell as an initial template, we systematically adjusted the lattice parameters and cell angles within the ranges allowed by the SAED constraints and, for each trial geometry, performed full variable-cell relaxations. For every relaxed configuration, the corresponding diffraction pattern was simulated and quantitatively compared with the experimental SAED data. Through this iterative procedure, we identified a structure whose simulated diffraction spots closely reproduce the measured zone-axis patterns and which, at the same time, lies at a local minimum of the DFT total energy, i.e., a thermodynamically metastable phase consistent with the Si-XIII assignment.

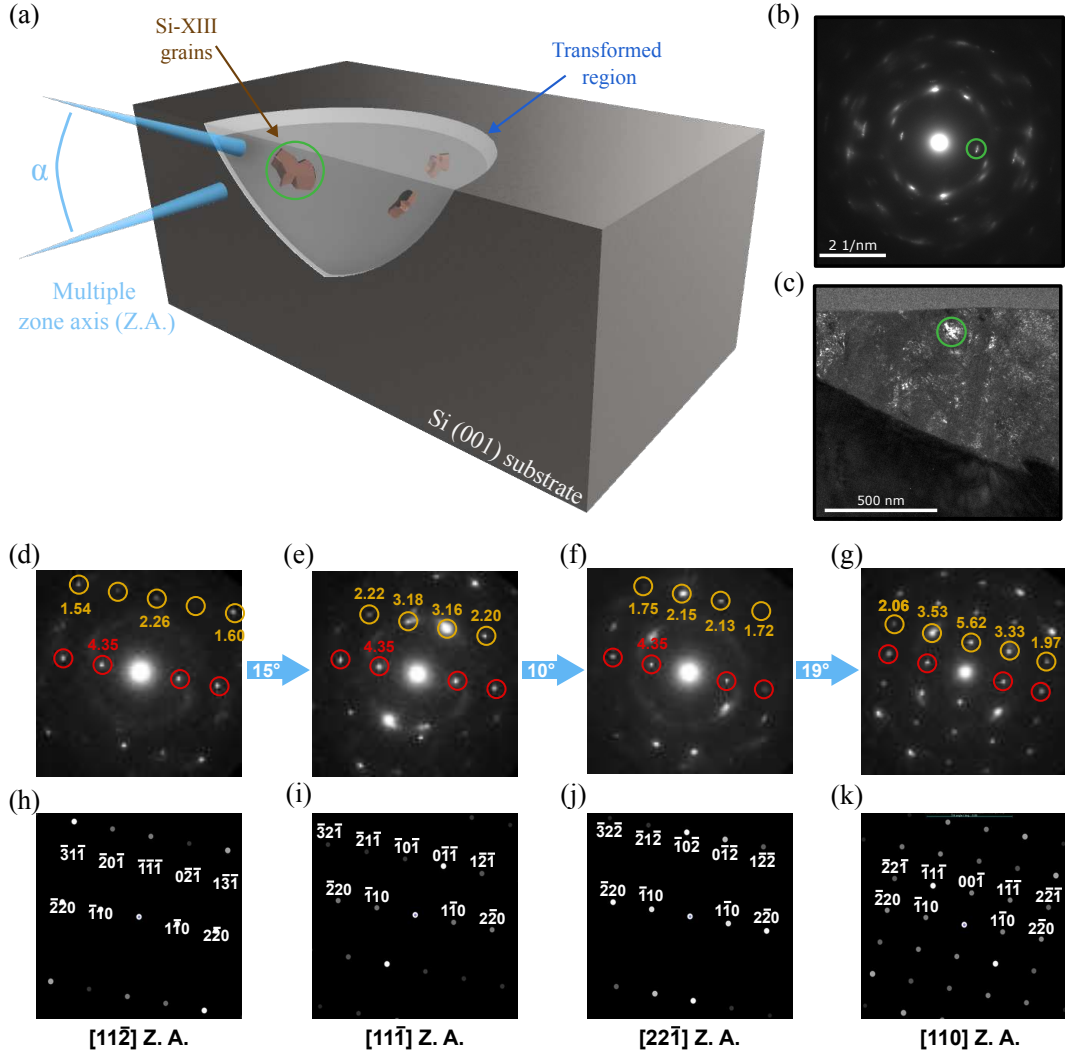


Figure 1: (a) Schematic representation of the experimental procedure employed to identify the crystal structure of the Si-XIII phase. One grain of the Si-XIII phase was selected inside the transformed region in the annealed pit. This grain was observed along multiple zone axis with mutual rotation of specific angles α . (b) SAED pattern of the transformed region in the pit (c) Dark Field TEM obtained from the reflection marked by the green circle in (b). The green circle highlights the selected Si-XIII crystal. (d),(e),(f) and (g) SAED patterns acquired from the same crystalline grain, marked by the green circle in (c), across multiple zone axes, with indicated mutual rotation angles. In these experimental patterns, the corresponding plane spacing distance is reported in \AA , for the main reflections. The sequence shows the systematic tilting procedure used to map the reciprocal lattice and the very good agreement with the proposed cell structure, as demonstrated by the corresponding simulated SAED (h),(i),(j), and (k), in which the pattern indexing is also reported.

The relaxed Si-XIII structure consistently converges to a triclinic cell with space group $P\bar{1}$ (No. 2) for all exchange-correlation functionals considered (complete details are provided in the Methods section). The corresponding equilibrium lattice parameters obtained with LDA, PBEsol, PBE, and SCAN are summarized in Table 1, together with the refined experimental values extracted from SAED. As expected, LDA yields the most compact cell, PBE the largest volume, while PBEsol and SCAN provide intermediate values. Starting from the DFT-relaxed cells, we re-simulated the SAED patterns and found that, in particular, the SCAN- and PBEsol-based structures reproduce the experimental diffraction spots with excellent accuracy. A subsequent fine-tuning of the lattice parameters to optimize the agreement with the measured SAED pattern led to the “Experimental” values reported in Table 1. In all cases, the eight-atom unit cell is composed of silicon

XC / data set	a [Å]	b [Å]	c [Å]	α [°]	β [°]	γ [°]	V [Å ³ /atom]
LDA	5.150	5.745	6.204	109.1	100.0	107.1	19.78
PBEsol	5.200	5.797	6.263	109.1	100.0	107.0	20.35
PBE	5.225	5.828	6.297	109.0	100.0	107.0	20.70
SCAN	5.191	5.807	6.266	109.1	100.0	107.0	20.38
Experimental	5.20	5.74	6.21	109	100	107	20.00

Table 1: Equilibrium lattice parameters of the proposed Si-XIII structure obtained from DFT relaxations with different exchange-correlation functionals, together with refined experimental values from SAED. The space group is $P\bar{1}$ (No. 2) with 8 atoms per unit cell. Wyckoff Positions are provided in Table S1 of the Supporting Information.

atoms occupying general Wyckoff $2i$ positions of $P\bar{1}$, with no additional symmetry-imposed constraints on the internal coordinates (full fractional coordinates are reported in the Supporting Information, Table S1).

The equilibrium density of this structure lies much closer to those of the cubic and hexagonal diamond phases than to the low-density R8 and BC8 metastable phases. Its DFT formation energy exceeds that of the stable diamond phases by $\Delta E \approx 100 - 120$ meV/atom but remains lower than R8 by $\Delta E \approx 20 - 90$ meV/atom (details are reported in the Supporting Information, Table S2), positioning Si-XIII as a competitive metastable allotrope, as also shown in Figure 2(b). To the best of our knowledge, this crystal structure has not been reported previously in either theoretical predictions or experimental studies, and thus represents a genuinely new allotrope that naturally emerges as the resolution for the long-sought Si-XIII phase.

2.1.3. Raman characterization and modeling

To validate this structural assignment, we compare experimental and theoretically computed Raman spectra. Gogotsi and Domnich [15] first assigned the Si-XIII label to an unknown phase observed after nanoindentation at 150–200 °C, characterized by distinctive Raman peaks at 200, 330, 475, and 497 cm^{-1} that could not be attributed to *dc*-Si, BC8, R8, or amorphous silicon. Subsequently, several other studies confirmed these Raman signatures for phases recovered after indentation-induced high-pressure transformations and subsequent annealing [4, 16, 19, 20].

However, a 2009 theoretical study [21], based on classical molecular dynamics simulations using the Tersoff potential (whose limitations in the present context are discussed in [22]), mislabeled a six-fold coordinated, high-density silicon phase observed during indentation simulations as Si-XIII. This misnaming has since been perpetuated in several theoretical works, despite the fact that the computationally predicted structure bears no relation to the experimentally observed Si-XIII phase recovered after annealing. The structure proposed here, after DFT optimization, finally reconciles the experimental observations with a well-defined crystal structure, as confirmed by the Raman validation discussed below.

The Raman spectra of the sample, both as-indentated and post-annealed, are presented in Figure 2 and compared with theoretical spectra derived from first-principles calculations. All peak frequencies are listed in Table 2, together with previous experimental reference values. The as-indentated spectrum of Figure 2(c) is consistent with analogous spectra we reported in Ref. [13], where the presence of BC8, R8, and deformed *dc*-Si phases was unambiguously identified by analyzing the measured Raman spectral intensity. We also showed that the scattering intensities of the Raman-active modes measured before annealing, which are related to phases different from *dc*-Si, are highest for perpendicular polarization configuration and lowest for parallel configuration (see Methods section). Hence, we focus here on the discussion of the data obtained in perpendicular configuration only (the interested reader can find the parallel configuration results in the Supporting Information Figure S3). This perpendicular configuration helps identify both R8 and BC8, although they appear after nanoindentation as a mixture [13] and still exhibit several peaks very close in frequency.

The peak frequencies obtained after fitting the as-indentated spectra (Table 2) are in excellent agreement with both previously reported experimental values [19, 23] and the calculated ones. Although the calculated frequencies suffer from a rigid shift due to the typical underestimation of Raman frequencies in LDA-DFT calculations [13], which is corrected in the theoretical peaks shown in Figure 2, the comparison allows for

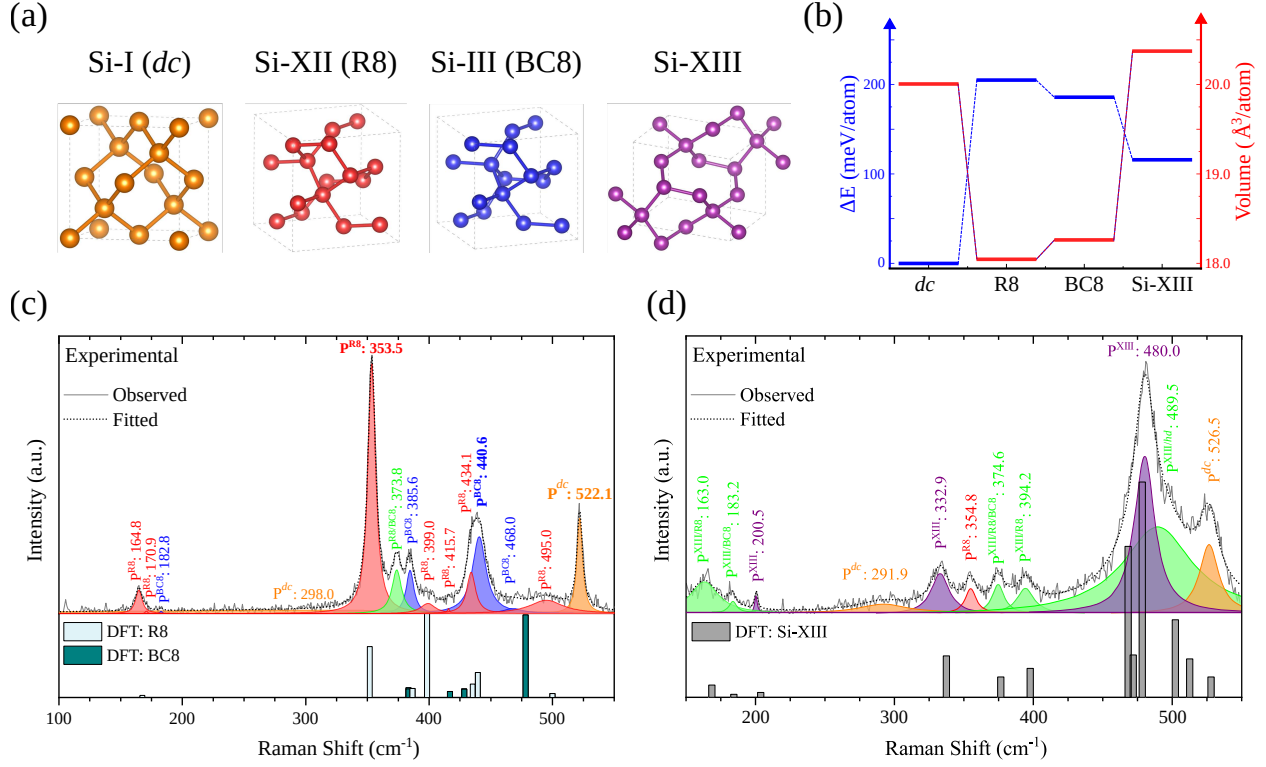


Figure 2: Raman spectroscopic analysis of silicon phases under nanoindentation and post-annealing. Panel (a) shows the crystal structures of the analyzed phases: *dc*-Si (orange), R8 (red), BC8 (blue), and Si-XIII (purple). Their formation energies and volumes are reported in panel (b). Fitted experimental polarized Raman spectra acquired in perpendicular configuration of 10 μm tip indented silicon are shown for (c) as-indentated and (d) post-annealed samples. Peak positions, intensities, and widths were treated as free parameters in the fitting procedure. Raman-active mode frequencies for the different phases, as reported in Table 2, were used as references. Experimental peaks are represented by Lorentzian functions colored according to the respective crystal structures shown in panel (a). DFT-calculated non-resonant Raman frequencies, shown as vertical lines in panels (c) and (d), have been rigidly shifted upward by 12 cm^{-1} to align the main R8 peak to the experimental one and facilitate comparison across all phases.

an unambiguous assignment of each peak to either BC8 or R8 (indicated by bold text in Table 2), except for the peak at approximately 374 cm^{-1} , which is shared between both phases.

Most of these Raman peaks disappear after thermal annealing, as shown in Figure 2(d), indicating a strong phase transition. Particularly, the two most intense peaks of R8 and BC8, found at approximately 354 and 441 cm^{-1} , respectively, exhibit minimal intensity (the former) or are completely absent (the latter). In fact, in Table 2, only a few Raman modes previously attributed to the R8/BC8 phases remain detectable and have marginal intensities. This suggests that some residual R8/BC8 phase is still present (confirmed by SAED and shown as Supporting Information in Figure S2), but with the majority of this mixture transformed into a crystallographically distinct structure.

Remarkably, the Raman mode shifts calculated for the proposed Si-XIII structure, shown together with the experimental spectra in Figure 2(d), perfectly match those corresponding to the peaks appearing *only* after the annealing process. Moreover, Table 2 shows that the frequencies of these theoretically predicted modes are in excellent agreement with previous reports on the, not identified yet, Si-XIII phase. Specifically, we find experimental peaks at approximately 200, 333, 480, and 490 cm^{-1} , all of which correspond to Raman modes calculated using DFT for our proposed Si-XIII structure. Noteworthy, these Raman mode shifts are in nearly perfect match with those reported in previous experiments at 200, 330, 475, and 497 cm^{-1} , respectively [15]. Although the peak at $\sim 480 \text{ cm}^{-1}$ is the most distinctive Raman fingerprint of the Si-XIII phase in our spectra, the peaks at 200 and 330 cm^{-1} , not present before annealing, can also unambiguously

Phase	Raman Mode	This work			Literature
		Exp. before ann.	Exp. after ann.	Theo.	Exp.[23]
<i>dc</i>	T _{2g}	522.1	526.5	513.4	520.3
R8	A _g	164.8	163.0	155.9	164.8
	E _g	170.9	-	163.0	170.0
	A _g	353.5	354.8	340.0	351.9
	E _g	373.8	374.6	374.6	373.3
	A _g	399.0	394.2	386.4	397.1
	A _g	415.7	-	423.4	412
	E _g	434.1	-	427.5	-
	E _g	495.0	489.5	487.9	-
BC8	T _g	182.8	183.2	155.1	182.4
	T _g	373.8	374.6	371.2	373.3
	A _g	385.6	-	371.3	384.2
	T _g	440.6	-	416.5	437.5
	E _g	468.0	-	466.2	463
Si-XIII	A _g	165.0	163	156.5	-
	A _g	-	183.2	172.4	-
	A _g	-	200.5	191.8	200
	A _g	-	332.9	325.5	330
	A _g	374.0	374.6	364.6	-
	A _g	-	394.2	385.7	-
	A _g	-	-	456.3	-
	A _g	-	-	459.9	-
	A _g	-	480.0	466.3	475
	A _g	-	489.5	490.3	497
	A _g	-	-	500.5	-
A _g	-	-	515.9	-	

Table 2: Comparison of experimental and theoretical Raman frequencies (in cm^{-1}) for various investigated silicon phases. The irreducible representations of the experimental phonon modes have been assigned through correspondence with the calculated modes. Previously reported experimental values for *dc*-Si, R8, and BC8 [23], as well as Si-XIII [15], are included for reference and are representative of the frequencies reported in other studies [16, 19, 24–27]. Experimental values from this work are highlighted in bold when the assignment is unique to a certain phase.

identify Si-XIII based on the DFT calculations .

Additionally, there are additional peaks at $\sim 163, 183, 375, 394,$ and 490 cm^{-1} that, based on our calculations, could also be attributed to Si-XIII, but are shared also with the BC8/R8 phases. Moreover, it is often difficult to identify single peaks and assign them to a specific phase, particularly in the $490 - 520 \text{ cm}^{-1}$ range. In fact, in this range, in addition to several possible peaks attributable to BC8/R8 or *dc*-Si, a couple of peaks attributable to *hd*-Si are also present [13]. Indeed, according to previous reports [16, 20], *hd*-Si is likely present in our samples after thermal annealing at 220°C . Consequently, the shoulder at approximately 500 cm^{-1} in our spectra, giving rise to the Lorentzian function at approximately 490 cm^{-1} shown in Figure 2d, may be attributed to a minimal fraction of *hd*-Si.

Finally, a peak located at approximately 522 cm^{-1} (526 cm^{-1}) is present before (after) annealing. This peak is certainly attributable to strained *dc*-Si not transformed into the metastable phases. However, the fact that its shift from the pristine phase peak expected at approximately 520 cm^{-1} increases after annealing suggests an increasing compressive strain acting on *dc*-Si, likely due to the expansion of the metastable phases upon annealing. This confirms the volume increase expected from the transition from the R8/BC8 mixture to the Si-XIII phase, in agreement with the calculated volumes reported in Table 1 and further discussed below.

2.2. Kinetics of the Si-XIII phase

2.2.1. Potential Energy Surface Exploration

The kinetics of the Si-XIII phase formation is then investigated to establish its connection to the main Si phases involved in these process conditions: *dc*, *hd*, R8, and BC8. Using extensive Potential Energy Surface (PES) explorations by means of the SS-Dimer method (see Methods section), we map the kinetic barriers connecting these phases, specifically focusing on the Si-XIII candidate structure.

Previous computational studies have attempted to find the Si-XIII phase or identify kinetic pathways for the *dc* phase transformations, exploiting a variety of approaches ranging from stochastic PES sampling to more sophisticated methods [28–33]. However, the exceptionally rich local-minima landscape of silicon makes these searches challenging: starting from *dc* or R8/BC8, one typically encounters a multitude of competing minima without naturally landing on a phase that simultaneously bridges the high-pressure and diamond-like PES neighborhoods. Here, initiating the search directly from Si-XIII reveals its pivotal role as the missing connecting phase between these energy basins, as clearly illustrated in the transition pathway network of Fig. 3.

The SS-Dimer search were performed starting from randomly displaced configurations of the Si-XIII candidate structure, with around 20000 repeated iterations. The details on the dimer iterations are provided in the Method section. The results were then analyzed and ordered by the height of the energy barrier to highlight the most relevant transitions. The same procedure was repeated with the other four phases under consideration: *dc*, *hd*, R8, and BC8. The final results are summarized in the Transition Pathway Network

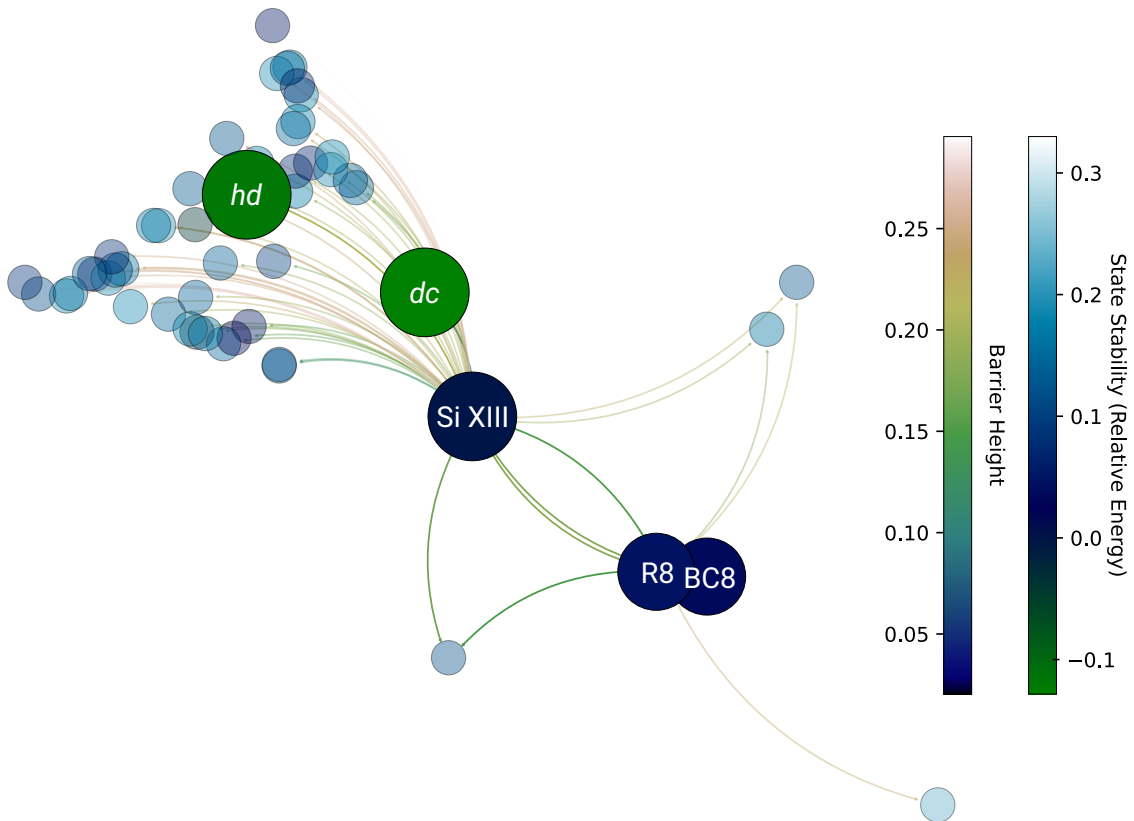


Figure 3: Transition Pathway Network showing the interconnection between the SI-XIII phase and the main known phases of silicon. The nodes of the network represent metastable minima while the edges connecting them represent the transition barrier found by the SS-Dimer method. The two colorbars represent the formation energy ΔE relative to the Si-XIII phase and the Barrier height for the transition connecting the two nodes. The relative length of the connection is proportional to the energy barriers of the transitions following the Kamada-Kawai representation.

of Figure 3, where circles represent metastable minima (with the most relevant ones highlighted by larger circles and the others shaded), and connecting lines represent the kinetic barriers. The data in the plot are arranged following the Kamada-Kawai algorithm [34], with line lengths proportional to the kinetic barrier heights between the connected minima. Transitions characterized by kinetic barriers higher than 0.3 eV/atom are not shown. Two color bars are reported for the height of the kinetic barrier and the formation energy of the energy minima, respectively.

The central role of Si-XIII in the kinetics of silicon phase transitions is evident from Figure 3: it acts as a connecting phase between the metastable R8/BC8 phases and the stable *dc* configuration. In fact, one result of our statistical investigation is that the transition path towards the Si-XIII phase represents the lowest kinetic pathway escaping from the energy basin of the R8 metastable phases. Additionally, we found a similar kinetic pathway that escapes from the BC8 phase and ends in the Si-XIII phase. The energy barriers associated with these transitions are: 111 meV/atom for the path connecting the R8 phase to the Si-XIII and 126 meV/atom for the one between the BC8 and the Si-XIII. These minimum energy paths are reported in Figure 4(a). These findings confirm the close relationship between the Si-XIII crystal structure and the R8 metastable phase, as already discussed from the crystallographic point of view in Section 2.1.1 and in Supplementary Figure S1.

Another interesting observation coming from our analysis is that the Si-XIII phase is very closely connected to the stable *dc* phase. We found three different transition pathways connecting these two phases (within our energy threshold for saddle point location), the lowest energy barrier carrying a barrier of only 90 meV/atom, significantly lower the other two higher paths (222 and 243 meV/atom), all reported in Figure 4(b). Additionally, we found an energy path connecting the Si-XIII and the *hd* phases. The energy barrier associated with this transition is 209 meV/atom. This indicates that the direct Si-XIII \rightarrow *dc* transition is dominant, although competitive pathways may occur under local residual strain still affecting the indentation region. Taken together, these results embed Si-XIII into a coherent kinetic framework, confirming a physically motivated argument for the proposed crystalline structure.

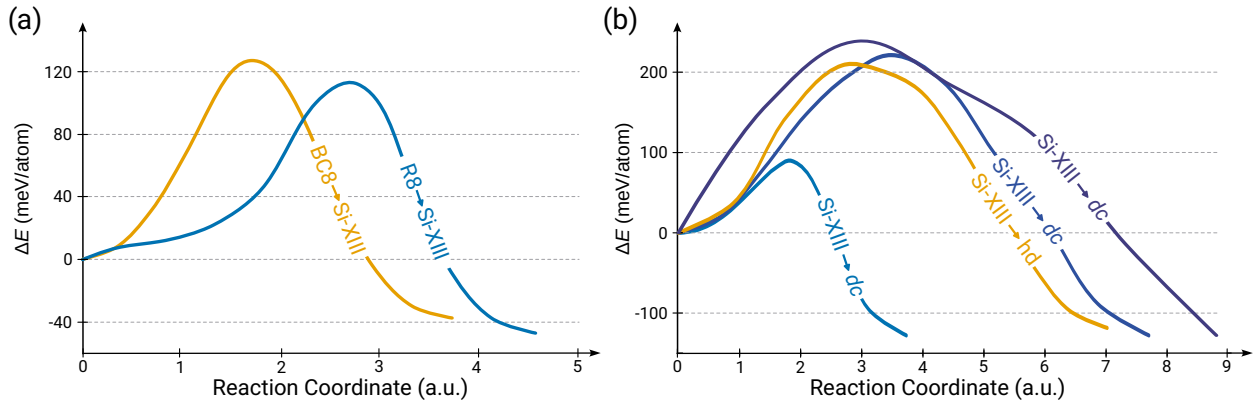


Figure 4: Minimum Energy Paths as calculated by Solid State Nudged Elastic Band connecting the Si-XIII phase to the main metastable phases of silicon. (a) Energy paths connecting the BC8 and R8 phases to the Si-XIII. (b) Energy paths connecting the Si-XIII phase to the *dc* and *hd* phases. The multiple paths found for the Si-XIII to *dc* transition are colored in shades of blue.

In order to validate these findings, in Figure 5, we report a Raman analysis of the post annealing evolution of the Si-XIII phase. First, the annealing procedure described in the Methods Section was reproduced on a silicon sample indented with a 20 μm spherical tip to produce the Si-XIII phase. We annealed the sample employing a heated stage holder up to 220°C, obtaining the result reported in Fig 5(a). The formation of the Si-XIII phase is clearly indicated by the Raman peak around the frequency of 480 cm^{-1} , and some minor ones at about 160 cm^{-1} and 200 cm^{-1} . In addition, a peak at 520 cm^{-1} clearly indicates the presence of *dc*, while a lesser intense peak around 500 cm^{-1} may indicate some presence of the *hd* phase [13]. Overall, these results are perfectly consistent with the ones reported in Figure 2(d), obtained with the 10 μm

spherical tip. We then used a second annealing procedure on this sample by placing it in a furnace at 250°C. The Raman analysis after this second annealing step is reported in Figure 5(b). The analysis shows a clear reduction in the peaks associated with the Si-XIII phase after this second annealing process. Only a broad peak around the frequency of 520 cm⁻¹ with a long tail towards lower frequencies remains after the second annealing. This peak is mainly attributed to the *dc* phase, with its long tail possibly indicating the presence of some *hd* phase. This additional experiment directly proves how the Si-XIII phase is not stable at 250°C and transforms to more stable phases, with its main reaction outputs being the *dc* and possibly the *hd* phases [16, 27]. Additionally, Atomic Force Microscopy (AFM) images, shown in Figure 5(c)-(e), also reveal significant differences in the indentation imprint heights after the first (stage annealing). This is because the volume of Si-XIII increases compared to the R8/BC8 phases. However, almost no change is observed in the imprint height after the second annealing at 250°C, confirming the volume similarity between Si-XIII and the Si diamond phases, as discussed previously.

These results perfectly validates the kinetic modeling described above, demonstrating the metastability

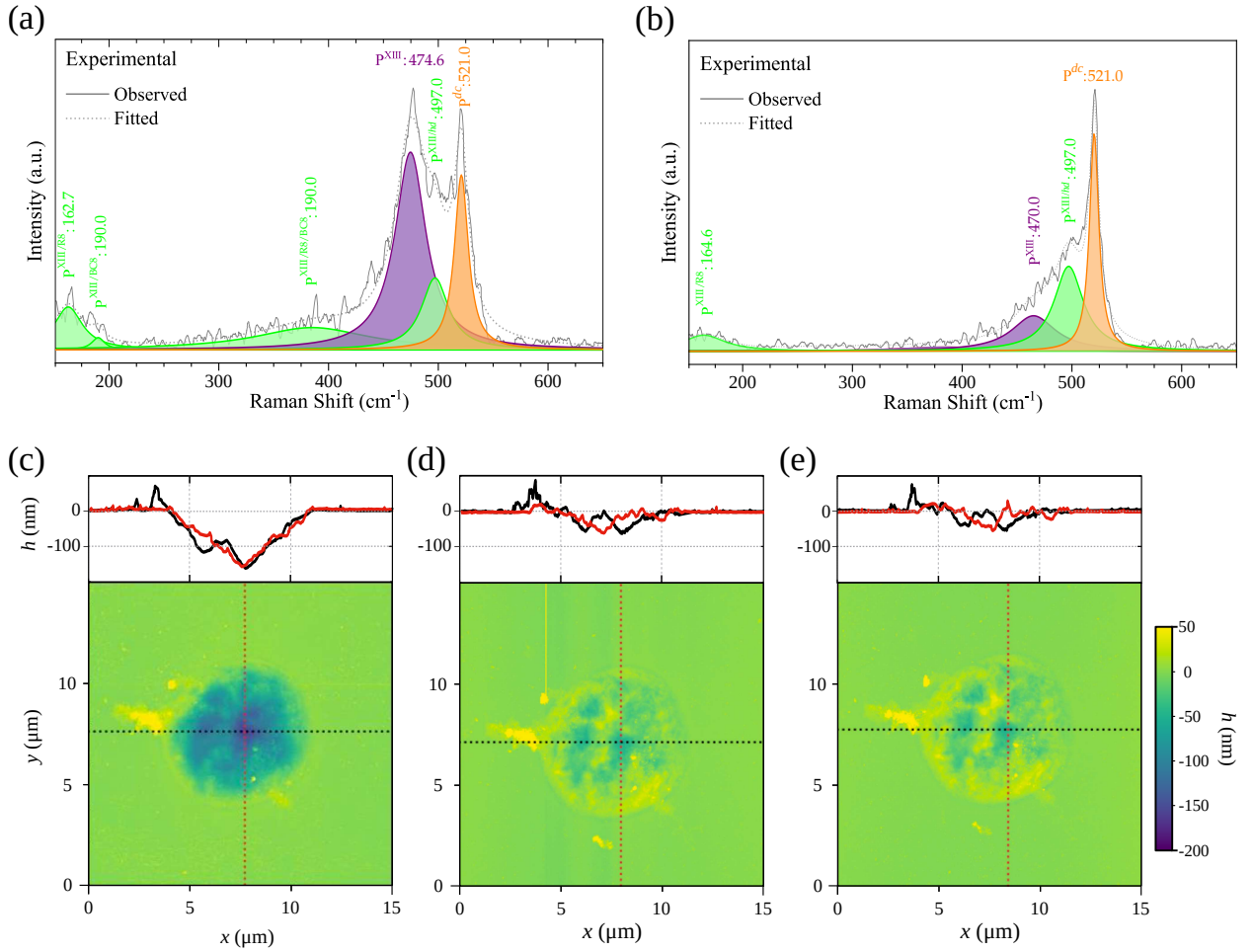


Figure 5: Analysis of the evolution of the Si-XIII phase before and after a second oven annealing. Fitted experimental polarized Raman spectra in perpendicular scattering geometry of 20 μm tip indented silicon are shown for a sample after a first stage annealing up to 220°C (a) and the same sample after a successive oven annealing up to 250°C (b). Peak positions, intensities, and widths were treated as free parameters in the fitting procedure. Raman-active mode frequencies for the different phases, as reported in Table 2 are used as references. Fitted peaks are represented by Lorentzian functions colored according to the respective crystal structures as in Figure 2. AFM maps for the same pit taken right after the indentation (c), after the first stage annealing (d) and after the final oven annealing (e).

of the Si-XIII phase and its main kinetic pathways linking it to the other Si phases.

3. Conclusions

In this work, we have resolved the long-standing question regarding the structural assignment of the Si-XIII phase, which was first observed over 20 years ago but has remained unidentified until now. Thanks to a convergent methodology, combining nanoindentation, systematic TEM/SAED analysis, and first-principles modeling, we have identified a triclinic $P\bar{1}$ structure with eight atoms per unit cell, crystallographically resembling the R8 metastable phase.

However, despite this geometric kinship, Si-XIII should not be regarded as merely a distorted variant of R8. Its equilibrium volume per atom is significantly larger, placing it much closer to the diamond phases, and its formation energy is intermediate between the R8/BC8 metastable phases and the stable diamond phases. Our PES exploration further confirms that it occupies a well-defined local minimum of the silicon energy landscape, with the R8 \rightarrow Si-XIII transition representing the lowest-barrier pathways escaping the R8 energy basin. This kinetic picture is directly confirmed by the experiments. The dominant Si-XIII \rightarrow dc transition, with a minimum barrier of only 90 meV/atom, naturally explains the thermal instability of Si-XIII observed above $\sim 250^\circ\text{C}$. Supplementary furnace annealing experiments corroborate this scenario, showing a clear reduction of Si-XIII Raman signatures and recovery toward the diamond phase, in agreement with the computed transition pathways. These findings establish the proposed Si-XIII phase as a kinetically and thermodynamically distinct phase in its own right.

The proposed structure achieves comprehensive agreement with all available experimental fingerprints of Si-XIII: interplanar spacings from multi-zone-axis SAED, characteristic Raman frequencies, and thermodynamic metastability that is fully consistent with the silicon phase diagram. To the best of our knowledge, this structure has not been previously reported in any theoretical or experimental study, representing a genuinely new silicon allotrope.

Beyond the specific case of Si-XIII, the challenge addressed here is a paradigmatic example of solid-solid phase transitions, demonstrating the power of integrating theoretical modeling with correlated experimental validation to resolve structural problems in complex materials systems.

4. Experimental Section/Methods

4.1. Nanoindentation

Nanoindentation was performed on monocrystalline silicon (001) using a KLA Corporation G200 System (Milpitas, CA, USA) equipped with spherical diamond indenter tips of 10 μm and 20 μm radii (Synton-MDP, Nidau, Switzerland). Loading proceeded at a constant strain rate $\dot{\epsilon} = 10^{-3} \text{ s}^{-1}$ [35, 36], while unloading was conducted at a constant rate of $\dot{P} = 1 \text{ mN/s}$ to promote crystalline phase transformation over amorphization [15, 37–39]. For the 20 μm tip, the maximum load was set at $P_{\text{max}} = 665 \text{ mN}$ to ensure complete phase transformation, while with the 10 μm tip, indentations were performed at approximately $P_{\text{max}} = 425 \text{ mN}$. Further experimental details are provided in Ref. [13]. Post-indentation thermal treatment was carried out on a temperature-controlled Raman stage under nitrogen flow. The annealing cycle comprised: (1) baseline measurement at 20 $^\circ\text{C}$, (2) heating to 220 $^\circ\text{C}$ (50 $^\circ\text{C}$), (3) stepwise cooling to 20 $^\circ\text{C}$ with Raman acquisition every 20 $^\circ\text{C}$, (4) second heating to 220 $^\circ\text{C}$ (50 $^\circ\text{C}/\text{min}$), and (5) final cooling to 20 $^\circ\text{C}$ (50 $^\circ\text{C}$). In a selected case, after completing the stage-based thermal cycling and Raman characterization, supplementary furnace annealing was performed at 250 $^\circ\text{C}$ for 2 h in a quartz tube under a nitrogen atmosphere, after which the sample was cooled to room temperature in air.

4.2. TEM, SAED, STEM

Transmission electron microscopy (TEM) and selected area electron diffraction (SAED) were performed using a JEOL JEM-2010F microscope equipped with a Schottky field emission gun operating at 200 keV. Cross-sectional lamellae were prepared by focused ion beam (FIB) milling in a Thermo Scientific™ Helios™ 5 UC DualBeam system using 30 keV Ga^+ ions, followed by low-energy (2 keV Ga^+) polishing to minimize

FIB-induced amorphization. The electron diffraction patterns were interpreted using the JEMS version 4.13531u2024b31 software (JEMS-SAS, Pierre Stadelmann, Switzerland).

4.3. Raman Spectroscopy

Raman measurements were conducted using a Renishaw inVia system with 532 nm excitation in back-scattering configuration, with the incident laser aligned along the substrate’s [001] crystallographic direction (z-axis). The setup features a polarizer and analyzer pair, with two half-wave plates enabling independent control of the excitation polarization angle α and analyzer orientation (parallel or perpendicular). Samples were oriented with the substrate’s $x' = [110]$ direction aligned to $\alpha = 0^\circ$. Polarization-resolved spectra were systematically acquired in both parallel ($\alpha = 0^\circ$) and perpendicular ($\alpha = 90^\circ$) configurations throughout the thermal cycling to track phase transformations and crystallographic evolution.

4.4. Atomic Force Microscopy

Atomic force microscopy (AFM) images were recorded using a Dimension ICON from Bruker in tapping mode. using Bruker TESPA VS-SS probes, featuring a nominal tip radius of approximately 5 nm. Image analysis and rendering has been carried out using the freeware Gwyddion software (<https://gwyddion.net/>)

4.5. First-Principles Calculations

DFT calculations were carried out with the Quantum ESPRESSO package [40]. The exchange-correlation functional was treated primarily with the local density approximation (LDA) [41]. For benchmarking purposes, the Perdew-Burke-Ernzerhof (PBE) generalized gradient approximation (GGA) [42], the strongly constrained and appropriately normed (SCAN) meta-GGA [43, 44] via the LIBXC library [45], and the PBEsol functional optimized for solids [46] were also tested.

Electron-ion interactions were described using norm-conserving Hartwigesen-Goedecker-Hutter [47, 48] pseudopotentials for LDA, PBE, and SCAN calculations, while the PBEsol case employed a pseudopotential from the standard Quantum ESPRESSO library [40]. A plane-wave basis set with a kinetic energy cutoff of 80 Ry was employed. Brillouin zone integration was performed using an $8 \times 8 \times 8$ Γ -centered k-point mesh following the Monkhorst-Pack scheme [49].

Structural relaxations were performed using variable-cell optimization until residual forces fell below 1 meV/Å and stress tensor components fell below 0.02 kbar, with self-consistent field convergence set to 10^{-10} eV. Dynamical stability and phonon dispersion relations were assessed via density functional perturbation theory (DFPT) [50]. Non-resonant Raman spectra, including mode frequencies and scattering intensities, were computed within the DFPT framework as implemented in Quantum ESPRESSO.

The VESTA software [51] and the Materials Project toolkit [52] were employed to display and manipulate crystal structures, while the crystal symmetry analysis was performed using the Materials Project toolkit [52] and the XRDlicious point defect submodule [53]

4.6. Potential Energy Surface Exploration

Potential Energy Surface (PES) explorations were carried out by repeated iterations of the Solid State Dimer (SS-Dimer) method [18]. We performed a total of about 100000 dimer searches with random initial displacements starting from the PES minima of each considered phase. As it would be unfeasible to perform such an extended analysis within an ab-initio framework, PES calculations were performed exploiting the GAP machine-learning interatomic potential for Si [54], which was recently shown to be particularly reliable in describing the kinetics of phase transitions in silicon [22, 55]. Initially, we optimised all relevant Si phases including the candidate Si-XIII structure. The thermodynamic properties predicted by the GAP potential and DFT, particularly using the PBE functional, showed excellent agreement as demonstrated in Table S2 in the Supporting Information.

More technically, we initialized the dimer iterations by performing small displacements of the atomic positions only, the cell parameters only, and both combined. The amplitude of the displacements was varied, sampling from a normal distribution with a standard deviation in the range of $[0.01 - 0.3]$ Å to sample in the

most uniform and complete way the neighborhood of the PES. We selected a maximum energy threshold for saddle point location of 300 meV/atom. To avoid artifacts arising from the dimer being displaced from the initial energy basin, we energy-optimized the two replicas in the converged dimer for each saddle point found to ensure connectivity with the initial energy minimum. The resulting kinetic database was then analyzed and ordered by energy barrier values to highlight the most physically-relevant transitions. Specific paths were also re-evaluated by Solid State Nudged Elastic Band (SS-NEB) [56] calculations initialized with the saddle point and the two minima found by the SS-Dimer calculation. This allowed us to draw the Minimum Energy Paths and evaluate the transition images in between the two connected minima. The energy convergence for saddle point location and for the minimization of the Dimer images was set to 10^{-3} eV/Å and 10^{-4} eV/Å, respectively. The TSASE implementation [57] for the Atomic Simulation Environment (ASE) [58] of the SS-Dimer method was exploited in this work.

Acknowledgements

Fruitful discussions with Prof. Kenneth Beyerlein and Rasool Doostkam (Institut national de la recherche scientifique, Canada) are gratefully acknowledged.

F.R., F.M. and E.S. acknowledge the CINECA consortium under the ISCRA initiative for the availability of high-performance computing resources and support.

F.R., M.B., E.S., A.M.M. and M.Z. acknowledge financial support under the National Recovery and Resilience Plan (NRRP), Mission 4, Component 2, Investment 1.1, Call for tender No. 104 published on 2.2.2022 by the Italian Ministry of University and Research (MUR), funded by the European Union – NextGenerationEU – Project Title "SiGe Hexagonal Diamond Phase by nanoIndenTation (HD-PIT)", project number: 2022-NAZ-0098 – CUP H53D23000780001 and B53D23004120006 - Grant Assignment Decree No. 957 adopted on 30.06.2023 by the Italian Ministry of University and Research (MUR). D.S. acknowledges the support from "Ramón y Cajal" programme by the Spanish MICIU/AEI/10.13039/501100011033 and ESF+ (grant no. RYC2022-037186-I).

Part of this work, has been carried out within the Joint Lab "Intelligent electrooptical sensing" established between IHP-Leibniz Institute for High Performance Microelectronics and Roma Tre University.

References

- [1] Cagin Ekici, Elizaveta Semenova, Davide Bacco, and Yunhong Ding. *Silicon Quantum Photonics - Platform and Applications*, chapter 22, pages 599–650. John Wiley & Sons, Ltd, 2023.
- [2] Stefan Wippermann, Yuping He, Márton Vörös, and Giulia Galli. Novel silicon phases and nanostructures for solar energy conversion. *Applied Physics Reviews*, 3(4):040807, dec 2016.
- [3] Matt Beekman. New hopes for allotropes. *Materials Today*, 18(6):304–305, 2015.
- [4] Bianca Haberl, Timothy A. Strobel, and Jodie E. Bradby. Pathways to exotic metastable silicon allotropes. *Applied Physics Reviews*, 3(4):040808, 2016.
- [5] Hezhu Shao, Daquan Ding, Li Zhang, Chang-Kun Dong, and Hao Zhang. Thermoelectric performance in a Si allotrope with ultralow thermal conductivity: a first-principles study combining phonon-limited electronic transport calculations. *Materials Today Physics*, 27:100756, 2022.
- [6] Pei Zhang, Tao Ouyang, Chao Tang, Chaoyu He, Jin Li, Chunxiao Zhang, Ming Hu, and Jianxin Zhong. Thermoelectric properties of four typical silicon allotropes. *Modelling and Simulation in Materials Science and Engineering*, 26(8):085006, 2018.
- [7] Zeyu Liu, Na Tan, and Chao Tang. Thermoelectric performance of tetragonal silicon allotrope tP36-Si from first-principles study. *The European Physical Journal B*, 94(12):247, 2021.

- [8] Yiheng Shen, Dongyuan Ni, Yanyan Chen, Jie Sun, and Qian Wang. A penta-silicene nanoribbon-based 3D silicon allotrope with high carrier mobility and thermoelectric performance. *Physical Chemistry Chemical Physics*, 24(44):27413–27422, 2022.
- [9] Ha-Jun Sung, W.H. Han, In-Ho Lee, and K.J. Chang. Superconducting Open-Framework Allotrope of Silicon at Ambient Pressure. *Physical Review Letters*, 120(15):157001, 2018.
- [10] Duck Young Kim, Stevce Stefanoski, Oleksandr O. Kurakevych, and Timothy A. Strobel. Synthesis of an open-framework allotrope of silicon. *Nature Materials*, 14(2):169–173, 2015.
- [11] Qianqian Wang, Bo Xu, Jian Sun, Hanyu Liu, Zhisheng Zhao, Dongli Yu, Changzeng Fan, and Julong He. Direct band gap silicon allotropes. *Journal of the American Chemical Society*, 136(28):9826–9829, 2014.
- [12] Chaoyu He, Chunxiao Zhang, Jin Li, Xiangyang Peng, Lijun Meng, Chao Tang, and Jianxin Zhong. Direct and quasi-direct band gap silicon allotropes with remarkable stability. *Physical Chemistry Chemical Physics*, 18(14):9682–9686, 2016.
- [13] Mouad Bikerouin, Anna Marzegalli, Davide Spirito, Gerald J. K. Schaffar, Corrado Bongiorno, Fabrizio Rovaris, Mohamed Zaghoul, Agnieszka Anna Corley-Wiciak, Leo Miglio, Verena Maier-Kiener, Giovanni Capellini, Antonio Massimiliano Mio, and Emilio Scalise. Formation of micrometer-sized textured hexagonal silicon crystals via nanoindentation. *Small Structures*, 5:2400552, 2025.
- [14] Megha Sasidharan Nisha, Yadu Chandran, Abhay Abhimanyu Sagade, Viswanath Balakrishnan, Alexandre Courac, and Kiran Mangalampalli. Hexagonal silicon formation and its phase transformability. *Advanced Functional Materials*, 35(44):2425188, 2025.
- [15] Vladislav Domnich and Yury Gogotsi. Phase transformations in silicon under contact loading. *Reviews on Advanced Materials Science(Russia)*, 3(1):1–36, 2002.
- [16] Sherman Wong, Brett C. Johnson, Bianca Haberl, Alfredo Mujica, Jennifer C. McCallum, and J. S. Williams. Thermal evolution of the indentation-induced phases of silicon. *Journal of Applied Physics*, 126(10):105901, 2019.
- [17] Graeme Henkelman and Hannes Jónsson. A dimer method for finding saddle points on high dimensional potential surfaces using only first derivatives. *The Journal of Chemical Physics*, 111(15):7010–7022, 1999.
- [18] Penghao Xiao, Daniel Sheppard, Jutta Rogal, and Graeme Henkelman. Solid-state dimer method for calculating solid-solid phase transitions. *The Journal of Chemical Physics*, 140(17):174104, 05 2014.
- [19] S. Ruffell, B. Haberl, S. Koenig, J. E. Bradby, and J. S. Williams. Annealing of nanoindentation-induced high pressure crystalline phases created in crystalline and amorphous silicon. *Journal of Applied Physics*, 105(9), 2009.
- [20] Bianca Haberl, Malcolm Guthrie, Stanislav V. Sinogeikin, Guoyin Shen, James S. Williams, and Jodie E. Bradby. Thermal evolution of the metastable r8 and bc8 polymorphs of silicon. *High Pressure Research*, 35(2):99–116, apr 2015.
- [21] K Mylvaganam, L C Zhang, P Eyben, J Mody, and W Vandervorst. Evolution of metastable phases in silicon during nanoindentation: mechanism analysis and experimental verification. *Nanotechnology*, 20(30):305705, July 2009.
- [22] Guojia Ge, Fabrizio Rovaris, Daniele Lanzoni, Luca Barbisan, Xiaobin Tang, Leo Miglio, Anna Marzegalli, Emilio Scalise, and Francesco Montalenti. Silicon phase transitions in nanoindentation: Advanced molecular dynamics simulations with machine learning phase recognition. *Acta Materialia*, 263:119465, 2024.

- [23] BC Johnson, Bianca Haberl, JE Bradby, Jeffrey C McCallum, and JS Williams. Temperature dependence of raman scattering from the high-pressure phases of si induced by indentation. *Physical Review B—Condensed Matter and Materials Physics*, 83(23):235205, 2011.
- [24] Sherman Wong, Bianca Haberl, BC Johnson, Andres Mujica, Malcolm Guthrie, Jeffrey C McCallum, JS Williams, and JE Bradby. Formation of an r8-dominant si material. *Physical Review Letters*, 122(10):105701, 2019.
- [25] LA Smillie, Marika Niihori, Ludovic Rapp, Bianca Haberl, James S Williams, Jodie E Bradby, Chris J Pickard, and Andrei V Rode. Exotic silicon phases synthesized through ultrashort laser-induced microexplosion: Characterization with raman microspectroscopy. *Physical Review Materials*, 4(9):093803, 2020.
- [26] Sowjanya Mannepalli and Kiran SRN Mangalampalli. In-situ high temperature micro-raman investigation of annealing behavior of high-pressure phases of si. *Journal of Applied Physics*, 125(22), 2019.
- [27] Daibin Ge, Vladislav Domnich, and Yury Gogotsi. Thermal stability of metastable silicon phases produced by nanoindentation. *Journal of Applied Physics*, 95(5):2725–2731, 2004.
- [28] Qiang Zhu, Artem R. Oganov, Andriy O. Lyakhov, and Xiaoxiang Yu. Generalized evolutionary metadynamics for sampling the energy landscapes and its applications. *Physical Review B - Condensed Matter and Materials Physics*, 92(2), 2015.
- [29] Li Zhu, R. E. Cohen, and Timothy A. Strobel. Phase Transition Pathway Sampling via Swarm Intelligence and Graph Theory. *Journal of Physical Chemistry Letters*, 10(17):5019–5026, 2019.
- [30] Andrés Mujica, Chris J. Pickard, and Richard J. Needs. Low-energy tetrahedral polymorphs of carbon, silicon, and germanium. *Physical Review B - Condensed Matter and Materials Physics*, 91(21):1–13, 2015.
- [31] Yansun Yao and Dennis D. Klug. Structural phase transitions in Si under hydrostatic and uniaxial compression. *Physical Review B - Condensed Matter and Materials Physics*, 85(21):1–5, 2012.
- [32] Jörg Behler, Roman Martoňák, Davide Donadio, and Michele Parrinello. Metadynamics simulations of the high-pressure phases of silicon employing a high-dimensional neural network potential. *Physical Review Letters*, 100(18), 2008.
- [33] Zhisheng Zhao, Fei Tian, Xiao Dong, Quan Li, Qianqian Wang, Hui Wang, Xin Zhong, Bo Xu, Dongli Yu, Julong He, Hui Tian Wang, Yanming Ma, and Yongjun Tian. Tetragonal allotrope of group 14 elements. *Journal of the American Chemical Society*, 134(30):12362–12365, 2012.
- [34] Tomihisa Kamada and Satoru Kawai. An algorithm for drawing general undirected graphs. *Information Processing Letters*, 31(1):7–15, 1989.
- [35] A. Leitner, V. Maier-Kiener, and D. Kiener. Essential refinements of spherical nanoindentation protocols for the reliable determination of mechanical flow curves. *Materials & Design*, 146:69–80, 2018.
- [36] Daniel Kiener, Michael Wurmshuber, Markus Alfreider, Gerald J. K. Schaffar, and Verena Maier-Kiener. Recent advances in nanomechanical and in situ testing techniques: Towards extreme conditions. *Current Opinion in Solid State and Materials Science*, 27(6):101108, 2023.
- [37] Chuanlong Lin, Xuqiang Liu, Dongliang Yang, Xiaodong Li, Jesse S Smith, Bihan Wang, Haini Dong, Shourui Li, Wenge Yang, and John S Tse. Temperature- and rate-dependent pathways in formation of metastable silicon phases under rapid decompression. *Physical Review Letters*, 125(15):155702, 2020.
- [38] Gerald J. K. Schaffar, Johann Kappacher, Daniel Tscharnuter, and Verena Maier-Kiener. The Phase Transformation of Silicon Assessed by an Unloading Contact Pressure Approach. *JOM*, 74(6):2220–2230, 2022.

- [39] Tom Juliano, Vladislav Dornich, and Yury Gogotsi. Examining pressure-induced phase transformations in silicon by spherical indentation and Raman spectroscopy: A statistical study. *Journal of Materials Research*, 19(10):3099–3108, 2004.
- [40] Paolo Giannozzi, Oscar Baseggio, Pietro Bonfà, Davide Brunato, Roberto Car, Ivan Carnimeo, Carlo Cavazzoni, Stefano De Gironcoli, Pietro Delugas, Fabrizio Ferrari Ruffino, et al. Quantum espresso toward the exascale. *The Journal of chemical physics*, 152(15), 2020.
- [41] Walter Kohn and Lu Jeu Sham. Self-consistent equations including exchange and correlation effects. *Physical review*, 140(4A):A1133, 1965.
- [42] John P Perdew, Kieron Burke, and Matthias Ernzerhof. Generalized gradient approximation made simple. *Physical review letters*, 77(18):3865, 1996.
- [43] Jianwei Sun, Adrienn Ruzsinszky, and John P Perdew. Strongly constrained and appropriately normed semilocal density functional. *Physical review letters*, 115(3):036402, 2015.
- [44] Yi Yao and Yosuke Kanai. Plane-wave pseudopotential implementation and performance of scan meta-gga exchange-correlation functional for extended systems. *The Journal of chemical physics*, 146(22), 2017.
- [45] Susi Lehtola, Conrad Steigemann, Micael JT Oliveira, and Miguel AL Marques. Recent developments in libxc—a comprehensive library of functionals for density functional theory. *SoftwareX*, 7:1–5, 2018.
- [46] John P Perdew, Adrienn Ruzsinszky, Gábor I Csonka, Oleg A Vydrov, Gustavo E Scuseria, Lucian A Constantin, Xiaolan Zhou, and Kieron Burke. Restoring the density-gradient expansion for exchange in solids and surfaces. *Physical review letters*, 100(13):136406, 2008.
- [47] S. Goedecker and M. Teter. Separable dual-space Gaussian pseudopotentials. *Physical Review B - Condensed Matter and Materials Physics*, 54(3):1703–1710, 1996.
- [48] C Hartwigsen, S Goedecker, and J Hutter. Relativistic separable dual-space Gaussian pseudopotentials from H to Rn. *Physical Review B*, 58(7):3641–3662, aug 1998.
- [49] Hendrik J Monkhorst and James D Pack. Special points for brillouin-zone integrations. *Physical review B*, 13(12):5188, 1976.
- [50] Stefano Baroni, Stefano De Gironcoli, Andrea Dal Corso, and Paolo Giannozzi. Phonons and related crystal properties from density-functional perturbation theory. *Reviews of modern Physics*, 73(2):515, 2001.
- [51] Koichi Momma and Fujio Izumi. *VESTA3* for three-dimensional visualization of crystal, volumetric and morphology data. *Journal of Applied Crystallography*, 44(6):1272–1276, Dec 2011.
- [52] Anubhav Jain, Shyue Ping Ong, Geoffroy Hautier, Wei Chen, William Davidson Richards, Stephen Dacek, Shreyas Cholia, Dan Gunter, David Skinner, Gerbrand Ceder, and Kristin A. Persson. Commentary: The materials project: A materials genome approach to accelerating materials innovation. *APL Materials*, 1(1):011002, 07 2013.
- [53] Miroslav Lebeda, Jan Drahokoupil, Petr Veřtát, Šimon Svoboda, Vojtěch Smola, Ubaid Ahmed, and Petr Vlčák. *XRDlicious*: an interactive web-based platform for online calculation of diffraction patterns and radial distribution functions from crystal structures. *Journal of Applied Crystallography*, 58(5):1810–1816, Oct 2025.
- [54] Albert P. Bartók, James Kermode, Noam Bernstein, and Gábor Csányi. Machine learning a general-purpose interatomic potential for silicon. *Phys. Rev. X*, 8:041048, Dec 2018.

- [55] Fabrizio Rovaris, Anna Marzegalli, Francesco Montalenti, and Emilio Scalise. Unraveling the atomic-scale pathways driving pressure-induced phase transitions in silicon. *Materials Today Nano*, 29:100548, 2025.
- [56] Daniel Sheppard, Penghao Xiao, William Chemelewski, Duane D. Johnson, and Graeme Henkelman. A generalized solid-state nudged elastic band method. *Journal of Chemical Physics*, 136(7), 2012.
- [57] <https://theory.cm.utexas.edu/tsase/>. Website of the TSASE code.
- [58] Ask Hjorth Larsen, Jens Jørgen Mortensen, Jakob Blomqvist, Ivano E Castelli, Rune Christensen, Marcin Dułak, Jesper Friis, Michael N Groves, Bjørk Hammer, Cory Hargus, Eric D Hermes, Paul C Jennings, Peter Bjerre Jensen, James Kermode, John R Kitchin, Esben Leonhard Kolsbjerg, Joseph Kubal, Kristen Kaasbjerg, Steen Lysgaard, Jón Bergmann Maronsson, Tristan Maxson, Thomas Olsen, Lars Pastewka, Andrew Peterson, Carsten Rostgaard, Jakob Schiøtz, Ole Schütt, Mikkel Strange, Kristian S Thygesen, Tejs Vegge, Lasse Vilhelmsen, Michael Walter, Zhenhua Zeng, and Karsten W Jacobsen. The atomic simulation environment—a python library for working with atoms. *Journal of Physics: Condensed Matter*, 29(27):273002, jun 2017.

Supplementary Information (SI): Resolving the Metastable Si-XIII Structure through Convergent Theory and Experiment

Fabrizio Rovaris^{a,1}, Corrado Bongiorno^{b,1}, Anna Marzegalli^a, Mouad Bikerouin^a, Davide Spirito^{c,f}, Gerald J. K. Schaffar^d, Mohamed Zaghoul^b, Agnieszka Anna Corley-Wiciak^c, Francesco Montalenti^a, Verena Maier-Kiener^d, Giovanni Capellini^{c,e}, Antonio M. Mio^b, Emilio Scalise^{a,*}

^a*Department of Materials Science. University of Milano Bicocca, Via R. Cozzi 55, 20125, Milano, Italy*

^b*Institute for Microelectronics and Microsystems (IMM). Consiglio Nazionale delle Ricerche (CNR), Strada VIII 5, 95121, Catania, Italy*

^c*IHP-Leibniz-Institut für innovative Mikroelektronik, Im Technologiepark 25, 15236, Frankfurt(Oder), Germany*

^d*Department of Materials Science. Montanuniversität Leoben, Roseggerstrasse 12, 8700, Leoben, Austria*

^e*Department of Science. Università Roma Tre, V.le G. Marconi 446, 00146, Rome, Italy*

^f*BCMaterials. Basque Center for Materials, Applications and Nanostructures, UPV/EHU Science Park, 48940, Leioa, Spain*

Table S1: Crystal structure of Si-XIII. Space group $P\bar{1}$ (No. 2), triclinic system, point group $\bar{1}$. All 8 atomic positions (fractional coordinates) of the primitive unit cell are listed; atoms are grouped in pairs related by the inversion center of the $2i$ Wyckoff site.

Atom	Wyckoff	x	y	z
Si ₁	$2i$	0.014	0.492	0.689
Si ₂	$2i$	0.986	0.508	0.311
Si ₃	$2i$	0.170	0.943	0.974
Si ₄	$2i$	0.830	0.057	0.026
Si ₅	$2i$	0.653	0.685	0.163
Si ₆	$2i$	0.347	0.315	0.837
Si ₇	$2i$	0.380	0.826	0.318
Si ₈	$2i$	0.620	0.174	0.682

*Corresponding author

¹This authors equally contributed

Phase	Approx.	a [Å]	b [Å]	c [Å]	α [°]	β [°]	γ [°]	V [Å ³ /atom]	ΔE [meV/atom]
<i>dc</i>	LDA	3.805	3.805	3.805	60.0	60.0	60.0	19.48	0
	PBEsol	3.842	3.842	3.842	60.0	60.0	60.0	20.05	0
	PBE	3.861	3.861	3.861	60.0	60.0	60.0	20.35	0
	SCAN	3.839	3.839	3.839	60.0	60.0	60.0	20.01	0
	GAP	3.861	3.861	3.861	60.0	60.0	60.0	20.36	0
R8	LDA	5.671	5.671	5.671	109.9	109.9	109.9	17.29	112
	PBEsol	5.720	5.720	5.720	109.9	109.9	109.9	17.73	116
	PBE	5.759	5.759	5.759	109.8	109.8	109.8	18.12	158
	SCAN	5.749	5.749	5.749	109.8	109.8	109.8	18.04	205
	GAP	5.749	5.749	5.745	109.6	109.6	109.6	18.16	175
	Exp.	5.63	5.63	5.63	109.8	109.8	109.8	16.94	-
BC8	LDA	5.670	5.670	5.670	109.5	109.5	109.5	17.54	124
	PBEsol	5.720	5.720	5.720	109.5	109.5	109.5	18.00	119
	PBE	5.758	5.758	5.758	109.5	109.5	109.5	18.37	157
	SCAN	5.747	5.747	5.747	109.5	109.5	109.5	18.26	186
	GAP	5.754	5.754	5.754	109.5	109.5	109.5	18.33	165
Si-XIII	LDA	5.150	5.745	6.204	109.1	100.0	107.1	19.78	98
	PBEsol	5.200	5.797	6.263	109.1	100.0	107.0	20.35	94
	PBE	5.225	5.828	6.297	109.0	100.0	107.0	20.70	98
	SCAN	5.191	5.807	6.266	109.1	100.0	107.0	20.38	116
	GAP	5.186	5.796	6.385	109.0	100.8	106.3	20.72	128
	Exp.	5.20	5.74	6.21	109	100	107	20.00	-

Table S2: Equilibrium lattice parameters of the proposed Si-XIII structure obtained from DFT relaxations with different exchange-correlation functionals and the GAP interatomic potential, compared to the metastable R8 and BC8 phases and the reference *dc*-Si. The atomic volume and cohesion energy are also reported, showing that the Si-XIII phase lies closer to the stable *dc*-Si, both in terms of volume and particularly in energy. For the Si-XIII and R8 phases, cell parameters in agreement with experimental SAED are also reported.

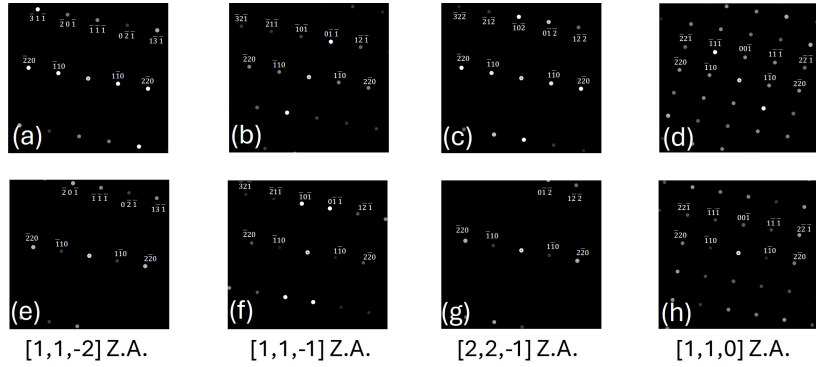


Figure S1: (a-d) Simulated SAED of the Si-XIII phase across multiple zone axes, as reported in Fig. 1(h-k). For comparison, the corresponding simulated SAED of the R8 phase is shown in panels (e-h). Indexing of the R8 phase is presented in the rhombohedral basis, as defined in Table S2

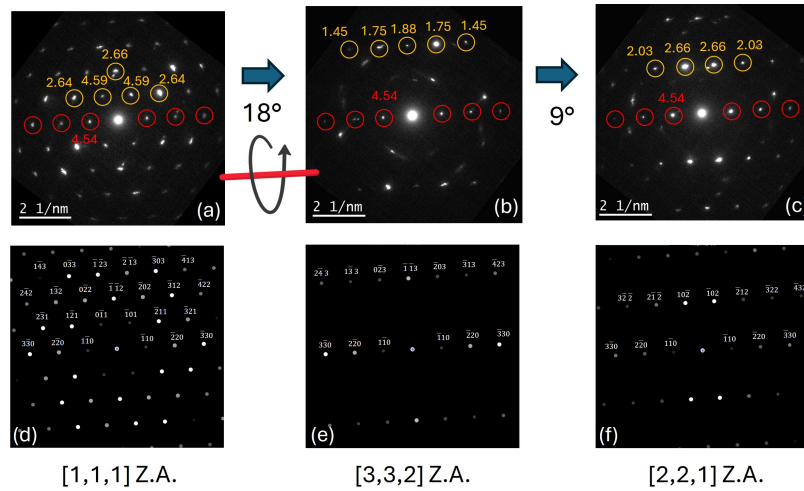


Figure S2: (a-c) SAED patterns acquired from the same crystalline grain across multiple zone axes, with indicated mutual rotation angles. In these experimental patterns, the corresponding plane spacing distance is reported in Å, for the main reflections. The sequence shows the systematic tilting procedure used to map the reciprocal lattice and a good agreement with the R8 cell structure, as demonstrated by the corresponding simulated SAED (d-f). Indexing of the R8 phase is presented in the rhombohedral basis, as defined in Table S2

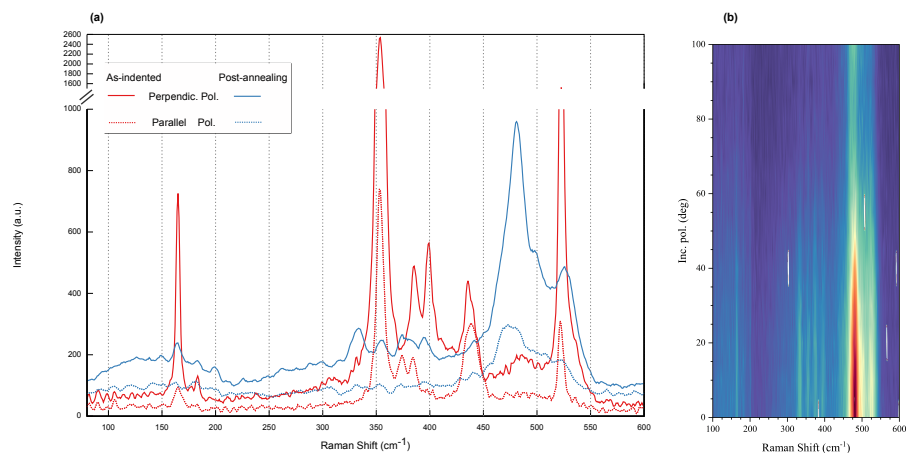


Figure S3: Raman spectra for indented silicon before and after annealing, both in parallel and perpendicular configuration (a). The spectrum after annealing and as a function of incidence polarization angle (α) is shown in (b).